

QUARTERLY JOURNAL OF THE ROYAL METEOROLOGICAL SOCIETY

Vol. 122

JANUARY 1996 Part B

No. 530

Q. J. R. Meteorol. Soc. (1996), **122**, pp. 327–355

Variational retrieval of humidity profile, wind speed and cloud liquid-water path with the SSM/I: Potential for numerical weather prediction

By L. PHALIPPOU*

European Centre for Medium-Range Weather Forecasts, UK

(Received 28 March 1995; revised 8 August 1995)

SUMMARY

Several regression algorithms have been proposed to retrieve geophysical parameters from the Special Sensor Microwave/Imager (SSM/I) radiances. Their performances are generally limited by a simplified handling of nonlinearities and/or by the poor quality of the a priori information. In this paper, a variational method is proposed for retrieving the atmospheric humidity profile, the wind speed and the cloud liquid-water path from SSM/I observations over ocean. This method is based on nonlinear optimal estimation theory. The first guess is derived from a European Centre for Medium-Range Weather Forecasts forecast, and the forecast-error covariance is used as a constraint. The geophysical variable space is mapped into the radiance space through a radiative-transfer model which permits an accurate representation of nonlinearities. This method has been applied to several orbits and the results for one of them are presented and discussed. It is argued that the variational approach is a simple optimal way of extracting information from SSM/I radiances, exploiting the high quality a priori information available from a numerical weather-prediction model. The retrieved humidity profiles are found to compare well with the total precipitable water estimated from a regression algorithm, while avoiding local bias in very dry and very wet conditions. It is also shown that the potential wind speed–cloud ambiguity is removed through the use of a high-quality wind speed first guess.

KEYWORDS: Cloud liquid-water Humidity Retrieval methods Satellite remote sensing SSM/I radiances Variational methods Wind speed

1. INTRODUCTION

The Special Sensor Microwave/Imager (SSM/I) is a seven-channel radiometer which operates in both vertical (V) and horizontal (H) polarizations at 19.35, 37 and 85.5 GHz and at 22.235 GHz where only the V polarization is available (Hollinger *et al.* 1990). Several atmospheric parameters can be retrieved from SSM/I observations (Hollinger 1991). Among them the total precipitable water vapour (TPW), surface marine wind speed (WS), cloud liquid-water path (CLW) and sea-ice are of primary interest for numerical weather prediction (NWP). These SSM/I products have been used for the validation of NWP fields (see, for instance, Liu *et al.* (1992), Phalippou (1992) and Tiedtke (1993)). Assimilation experiments of SSM/I TPW and/or WS have already been made in NWP models (see, for instance, Bloom and Atlas (1991), Filiberti (1993) and Wu and Derber (1994)). The results are encouraging, and Wu and Derber (1994) and Derber *et al.* (1994) envisaged assimilating SSM/I TPW and WS into the operational data-assimilation system of the National Meteorological Centre (NMC), a process that actually started in January 1995.

After the launch of the first SSM/I on board the F-8 satellite of the Defense Meteorological Satellite Program (USA), SSM/I TPW, WS and CLW were retrieved separately with regression algorithms (Hollinger 1991). Several problems were found in the products derived from the algorithms reported in Hollinger (1991), and many ‘improved’ regression

* Corresponding address: European Centre for Medium-Range Weather Forecasts, Shinfield Park, Reading, Berkshire RG2 9AX, UK.

algorithms have flourished afterwards. However, there is one critical point common to any of these regression methods: their performances are limited by a simplified handling of nonlinearities and/or by the poor quality of the a priori information. This problem is particularly critical when clouds are present in the field of view (FOV) as the retrieval problem becomes more nonlinear. More recently, Wentz (1992) and Greenwald *et al.* (1993) used a priori information coming from climatology and a simplified radiative-transfer model for inverting SSM/I radiances. The weakness of their approach is that the errors in the a priori information, in the radiances and in the radiative-transfer model, are not taken into account in the retrieval process.

Variational methods offer an alternative approach for the estimation of the geophysical parameters from SSM/I observations. The geophysical parameters are estimated simultaneously following the theory of optimal estimation, and are, therefore, the best set of parameters that explain the observed radiances, while being consistent with the available a priori information. In addition, an estimation of the errors of the 'retrieved' products can be computed and the quality control is easier. The variational method is used at the European Centre for Medium-Range Weather Forecasts (ECMWF) for the operational pre-processing and quality control of data from the TIROS* Operational Vertical Sounder (TOVS) and is called 1DVAR, as the temperature and humidity profile are retrieved along the vertical (Eyre *et al.* 1993). Recently, Prigent *et al.* (1994) applied a nonlinear estimation scheme for retrieving TPW, WS, CLW and rain rate from SSM/I observations with an additional horizontal smoothing constraint on the wind and TPW fields.

This paper presents the theory, the implementation and the results of a 1DVAR method for the estimation of the humidity profile, WS and CLW over oceans, using SSM/I observations and ECMWF forecast fields with their error covariances. The goal for this study is to demonstrate the feasibility of the variational method in a NWP environment for extracting geophysical information from SSM/I measurements in an optimal way. This study also fits into the ECMWF preparatory activities for the processing of the window and humidity channels of ATOVS (Advanced TOVS) data. The principle of the variational method is described in section 2. The a priori information coming from ECMWF fields, also called background, is described in section 3. The radiative-transfer model, its calibration and a sensitivity analysis are presented in section 4. The results, including the retrieved products, their theoretical accuracies and the quality control, are presented and discussed in section 5 for a situation representative of various meteorological conditions. Finally, a summary of the study and the conclusions are given in section 6.

2. THEORY

The principle of nonlinear optimal estimation in the context of satellite data assimilation has been discussed by Rodgers (1976) and Eyre (1989). Let us define \mathbf{x} as the state vector (hereafter called control variable) formed by the atmospheric and surface variables. We seek the best estimate of \mathbf{x} knowing the a priori or background vector \mathbf{x}^b given by the ECMWF first guess (see section 3) and the coincident SSM/I observation vector \mathbf{y}^o . We denote by $\mathbf{y}(\mathbf{x})$ the operator mapping the control variable \mathbf{x} into the observation (radiance) space \mathbf{y} , i.e. $\mathbf{y}(\mathbf{x})$ is the radiative-transfer model which calculates the radiances corresponding to the control variable \mathbf{x} . When the errors in the observations and the errors in the a priori information have Gaussian distributions and are uncorrelated, then the likelihood function (also called cost function) is given by:

$$\mathcal{J}(\mathbf{x}) = \frac{1}{2}(\mathbf{y}(\mathbf{x}) - \mathbf{y}^o)^T \cdot (\mathbf{O} + \mathbf{F})^{-1} \cdot (\mathbf{y}(\mathbf{x}) - \mathbf{y}^o) + \frac{1}{2}(\mathbf{x} - \mathbf{x}^b)^T \cdot \mathbf{B}^{-1} \cdot (\mathbf{x} - \mathbf{x}^b) \quad (1)$$

* Television Infra-Red Observation Satellite.

where \mathbf{O} is the expected error covariance of the observations, \mathbf{F} is the expected error covariance of the radiative-transfer model (forward operator), \mathbf{B} is the expected error covariance of the background \mathbf{x}^b , and the superscripts T and -1 denote matrix transpose and inverse respectively. By definition, the best estimate of \mathbf{x} corresponds to the maximum of the probability density function and is found by minimizing the cost function. The two terms in (1) represent the observation and the background costs and are often noted \mathcal{J}_o and \mathcal{J}_b in the literature. In this study \mathbf{x} is a 22-element vector which contains the Naperian logarithm of the specific-humidity profile on 20 levels, WS and CLW.

The Newton method has been used to find the minimum of the cost function. During the minimization process some elements of \mathbf{x} may take meaningless values (negative wind-speed values for instance). Bounds and physical constraints must then be applied to control such events. The Numerical Algorithms Group (NAG) minimization package E04LBF has been used in this study as it is built on a modified Newtonian iteration scheme which allows us to specify the bounds of \mathbf{x} (NAG 1991). The only lower bounds specified were on WS and CLW where the bounds were set to zero. The use of the logarithm of the specific humidity alleviates the lower-bound problem, but the humidity supersaturation still needs to be controlled. This has been achieved by adding an *ad hoc* constraint term $\mathcal{J}_{\text{sat}}(\mathbf{x})$ to the cost function (see section 3(b)). This gives a smoother solution than the NAG bound control, as explained in section 3(b).

The complete cost function $\mathcal{J}(\mathbf{x})$ to minimize is then written as:

$$\mathcal{J}(\mathbf{x}) = \mathcal{J}_o(\mathbf{x}) + \mathcal{J}_b(\mathbf{x}) + \mathcal{J}_{\text{sat}}(\mathbf{x}). \quad (2)$$

Note that the use of $\mathcal{J}_{\text{sat}}(\mathbf{x})$ modifies the probability density function of the unconstrained problem, and is similar to saying that the hypothesis of Gaussian errors is not valid when an element of \mathbf{x} is close to one of its bounds.

During the minimization the n th estimate of \mathbf{x} is calculated as follows:

$$\mathbf{x}_{n+1} = \mathbf{x}_n - [\mathbf{H}\{\mathcal{J}(\mathbf{x}_n)\}]^{-1} \cdot \nabla\{\mathcal{J}(\mathbf{x}_n)\} \quad (3)$$

where \mathbf{H} is the Hessian operator and ∇ is the gradient operator with respect to \mathbf{x} . The gradient of the cost function can be written analytically by differentiating (2):

$$\nabla(\mathcal{J}(\mathbf{x})) = \mathbf{K}\{\mathbf{x}\}^T \cdot (\mathbf{O} + \mathbf{F})^{-1} \cdot (\mathbf{y}\{\mathbf{x}\} - \mathbf{y}^o) + \mathbf{B}^{-1} \cdot (\mathbf{x} - \mathbf{x}^b) + \nabla(\mathcal{J}_{\text{sat}}(\mathbf{x})) \quad (4)$$

where

$$\mathbf{K}\{\mathbf{x}\} = \nabla(\mathbf{y}\{\mathbf{x}\}). \quad (5)$$

$\mathbf{K}\{\mathbf{x}\}$ is the Jacobian matrix, i.e. its elements are the partial derivatives of the simulated observations with respect to the control variable. Note that \mathbf{K} depends on \mathbf{x} since the problem is nonlinear.

The Hessian matrix is obtained by differentiating (4) with respect to \mathbf{x} . It has been shown that the gradient of the \mathbf{K} matrix can be neglected to approximate the Hessian matrix (Eyre *et al.* 1993) even when the problem is nonlinear. The Hessian matrix is then given approximately by:

$$\mathbf{H}(\mathcal{J}(\mathbf{x})) \approx \mathbf{B}^{-1} + \mathbf{K}\{\mathbf{x}\}^T \cdot (\mathbf{O} + \mathbf{F})^{-1} \cdot \mathbf{K}\{\mathbf{x}\} + \mathbf{H}(\mathcal{J}_{\text{sat}}(\mathbf{x})). \quad (6)$$

The a posteriori error-covariance matrix $\mathbf{S}(\mathbf{x}_n)$ of the estimation \mathbf{x}_n is equal to the inverse of the Hessian (Rodgers 1976). However, when the \mathbf{S} matrix is computed at the end of the minimization, care must be taken to use the Hessian of the unconstrained problem, i.e. the last term of (6) must be omitted. Otherwise the errors given by \mathbf{S} can be substantially

underestimated when the value of the constraint term (last term of (6)) is non-negligible with respect to the first two terms of (6). $\mathbf{S}(\mathbf{x}_n)$ is then approximated as follows:

$$\mathbf{S}(\mathbf{x}_n) \approx (\mathbf{B}^{-1} + \mathbf{K}\{\mathbf{x}_n\}^T \cdot (\mathbf{O} + \mathbf{F})^{-1} \cdot \mathbf{K}\{\mathbf{x}_n\})^{-1}. \quad (7)$$

\mathbf{S} not only provides an estimate of the variances of the retrieval errors (diagonal terms) but also provides the covariances between the errors through the off-diagonal terms.

3. ECMWF FIRST-GUESS FIELDS

The background \mathbf{x}_b used in this study is extracted from the ECMWF forecast-model fields. The general characteristics of the ECMWF data-assimilation scheme and the strategy we have taken to derive \mathbf{x}_b are presented in section 3(a). The choice of the elements which form \mathbf{x}_b and the related error-covariance matrix are presented in section 3(b).

(a) ECMWF data-assimilation cycle

The ECMWF operational data assimilation and forecast cycle is given in Fig. 1. The goal of the analysis is to provide the initial state of the atmosphere for the forecast model. Four analyses are made each day for 00, 06, 12, and 18 UTC. Observations from a 6-hour period spanning the nominal analysis time are used to correct a 6-hour forecast—called first guess (FG)—made from a previous analysis. Deviation of the observations from the first guess are analysed to give increment fields which are then added to the FG fields.

At the time of this study, the ECMWF analysis is built on an optimal interpolation method (Lorenc 1981). The analysis and the forecast model use the same coordinate system. The current ECMWF forecast model is spectral with triangular truncation at total wave number 213 (T213) which is equivalent to a 62 km mesh; 31 levels (L31) sample the atmosphere between the surface and 10 hPa. The ECMWF fields used in this study have been simulated for a T106/L31 configuration (125 km horizontal resolution) with the new experimental prognostic cloud scheme. For each SSM/I observation location, the background profile has been computed by interpolating in time and space the three FGs which spanned the SSM/I observation time. For that reason the background profile is often

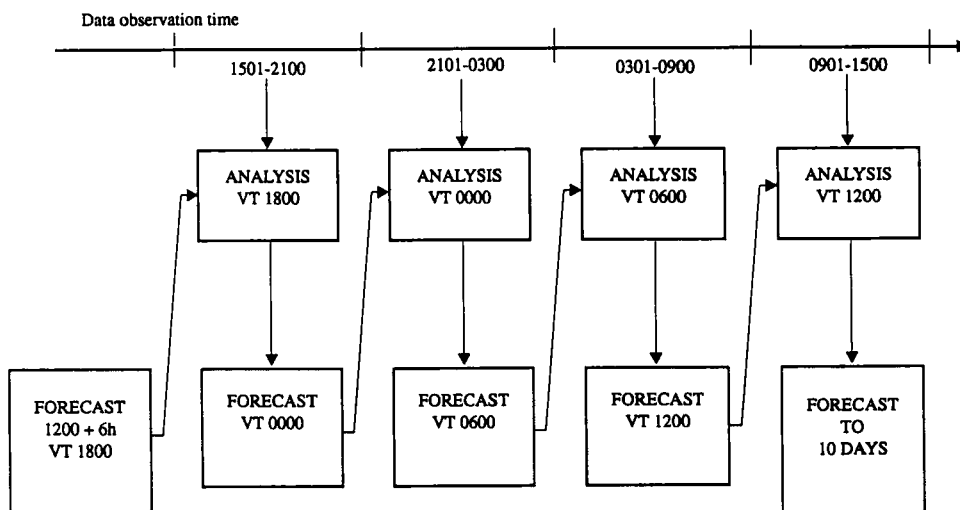


Figure 1. ECMWF operational data assimilation-forecast cycle. (VT = Valid Time).

called the first guess at the appropriate time (FGAT). Note that exactly the same strategy is used in the operational analysis for the TOVS data.

At the present time, for theoretical and technical reasons, the data-assimilation scheme can only assimilate cloud observations if they are a direct measure of the variables as used in the prognostic cloud scheme. Obviously, such measurements do not exist and, therefore, assimilation experiments for a given period (1 week to 1 month) were all started without cloud observations, i.e. no cloud was present for the first analysis of the first day of the experiment. During the subsequent analyses the cloud field produced by the forecast of the previous day was used as the 'pseudo-analysed' cloud field. This scheme was used in order to try to minimize the spin-up/spin-down humidity problem which would occur in the forecast if each analysis were started with a cloud field set to zero. The meteorological situation presented in section 5 took place three days after the beginning of the assimilation experiment period.

(b) *Control variable and background errors*

(i) *Humidity profile.* At SSM/I frequencies, the radiances at the top of the atmosphere depend on the atmospheric profile (humidity, temperature, cloud) and on surface conditions. However, the radiances do not exhibit the same sensitivity to each atmospheric parameter. A simple and objective way to select which parameters should be included in the control variable \mathbf{x} , is to analyse the information content of the radiances with respect to those parameters. This can be achieved, for instance, by comparing the diagonal elements of the error-covariance matrix of the background, i.e. \mathbf{B} , with the diagonal elements of the a posteriori expected error covariance \mathbf{S} given by (7). Although this method may present some limitations, because the off-diagonal terms of the matrices are not taken into account, it still gives a good insight for selecting the control variable. This method has been applied to a number of atmospheric conditions, using the \mathbf{B} matrix from the operational TOVS-1DVAR scheme (Eyre *et al.* 1993) for temperature and humidity. In these calculations SSM/I radiances improved mainly the error in the humidity-profile retrieval between the surface and 300 hPa, which corresponds to the ECMWF level 13. The first 19 elements of \mathbf{x} were set to the humidity profile on level 13 to 31 of the ECMWF model. The humidity at 2 m height has been added as the 20th element of \mathbf{x} . The rest of the atmospheric profile, i.e. the temperature profile and the humidity on levels 1 to 11, was used as parameters in the radiative-transfer model, but was not modified during the iterative retrieval.

The specific humidity (noted q in kg kg^{-1}) is the humidity prognostic variable of the ECMWF model. It typically varies by 2 to 3 orders of magnitude along a vertical profile or between a polar and a tropical profile. If q is used directly as a control variable then the error-covariance matrix \mathbf{B} depends on the background profile itself. If now one uses the Napierian logarithm of q ($\ln(q)$) as the control variable, then the range of variation is much more limited. It is then possible to have a single \mathbf{B} matrix for representing the ECMWF humidity FG error over the whole globe, whatever the atmospheric profile. Note that the use of a single \mathbf{B} is not ideal, but it is a better approximation for $\ln(q)$ than for q . This change of variable still retains some 'physical meaning' as shown by the relationship between $\ln(q_i)$ and the relative humidity (rh_i) at level i (at constant temperature):

$$dx_i = d(\ln(q_i)) = dq_i/q_i \approx d(rh_i)/rh_i. \quad (8)$$

For instance, (8) shows that a $dx_i = 0.1$ fractional change in q_i is equivalent to a 5% change in relative humidity when the relative humidity is equal to 50%. The elements of the background-error covariance matrix related to humidity have been derived from the \mathbf{B} matrix used in TOVS-1DVAR (see Table 1).

TABLE 1. BACKGROUND-ERROR CORRELATION MATRIX AND STANDARD DEVIATIONS ASSUMED FOR IDVAR

Correlation matrix of background error (*100):	
X	PRES
ln(q)	304
ln(q)	340
ln(q)	377
ln(q)	417
ln(q)	458
ln(q)	500
ln(q)	543
ln(q)	588
ln(q)	633
ln(q)	679
ln(q)	726
ln(q)	772
ln(q)	817
ln(q)	861
ln(q)	902
ln(q)	940
ln(q)	971
ln(q)	995
ln(q)	1009
ln(q)	1013
WS	
CLW	
Element	1 2 3 4 5 6 7 8 9 10 11 12 13 14 15 16 17 18 19 20 21 22
Standard deviation of background error (*100):	
	74 74 72 69 68 64 62 63 66 69 62 57 54 50 52 57 60 50 44 44 200 20

X: Control variable.
PRES: Pressure on ECMWF model levels for 1013 hPa surface pressure.
q: Specific humidity (kg kg⁻¹).
WS: Marine wind speed (m s⁻¹).
CLW: Cloud liquid-water path (kg m⁻²).

One of the advantages of using $\ln(q)$ is that this variable does not have a lower bound. However, the upper-bound problem still exists, and during the minimization of the cost function one has to check that the humidity profile is not too supersaturated. Although a constraint which limits the supersaturated humidity to be equal to the saturated seems attractive, it has been found that it has several drawbacks. Such a constraint introduces discontinuity in the trajectory of the minimization, which should generally be avoided. Secondly, as the saturation water vapour pressure depends only on the temperature, specifying a strict cut-off of the humidity at the saturated value implies that the temperature profile has no errors. Therefore, the following form has been preferred for the supersaturation constraint:

$$\mathcal{J}_{\text{sat}}(\mathbf{x}) = \sum_i \mathcal{J}_{\text{sat}}(x_i) \quad 1 \leq i \leq 20 \quad (9)$$

with:

$$\begin{aligned} \mathcal{J}_{\text{sat}}(x_i) &= c_i(x_i - x_i^{\text{sat}})^3 = c_i(\ln(q_i) - \ln(q_i^{\text{sat}}))^3 \quad \text{if } q_i \geq q_i^{\text{sat}} \\ \mathcal{J}_{\text{sat}}(x_i) &= 0 \quad \text{if } q_i < q_i^{\text{sat}} \end{aligned}$$

where q_i^{sat} is the specific humidity at saturation at level i , i.e. a function of temperature only (for a given pressure), and c is an ad hoc constant. This cubic form has been selected because it is not highly nonlinear (remember that the unconstrained cost function given by (1) is quadratic if the radiative-transfer model is linear) while permitting a nonlinear gradient. Note also that the first and second derivatives (gradient and Hessian) are continuous at the junction point $x_i = x_i^{\text{sat}}$.

The typical standard deviation of the FG temperature profile is around 1 K, which is equivalent to a 7% error in relative humidity. The constant c in the cost function \mathcal{J}_{sat} has been tuned such that a supersaturation up to 7% is permitted. We checked that after minimization with this humidity constraint only a few cases had relative humidity bigger than 107%.

(ii) *Clouds.* The primary benefit of having a cloud background field derived from NWP is that the vertical location and the extent of the cloud are given in a manner consistent with the physics and the dynamics of the atmosphere. For instance, this will ensure that clouds are located at the maximum of the relative-humidity profile. The cloud fraction and the cloud mixing ratio (defined as the ratio of liquid/ice mass to the mass of wet air) on each level are the prognostic variables of the new ECMWF prognostic cloud scheme. The cloud fraction is the geometrical fraction of the area defined by the ECMWF model grid which contains liquid or ice cloud. If the ECMWF cloud fraction were to be included in the control variable \mathbf{x} then an assumption would be needed for overlapping the cloud layers, since the model grid area and the typical SSM/I FOV size are in a ratio of 4:1. Although some overlap assumptions have been used for the radiative balance in the physical parametrization of the ECMWF forecasting model, there is no evidence that this assumption is suitable for the forward model in the microwave spectrum. So, the cloud fraction has not been included in the control variable. Similarly, if the cloud cover were supposed inhomogeneous at the SSM/I resolution, then the radiative-transfer model would need a parametrization of the cloud three-dimensional (3D) structure at the sub-FOV scale. This problem—often referred to as ‘beam filling effect’—is beyond the scope of this study, and the clouds have been assumed horizontally homogeneous which is consistent with the use of a radiative-transfer model in plane parallel atmosphere (see section 4). The resulting errors can be accounted for in the forward operator covariance matrix \mathbf{F} .

In order to perform the radiative-transfer simulation the liquid/ice profile of the cloud is required. Because of the lack of ‘ground truth’ it is quite difficult to assess the errors

of the ECMWF forecast cloud fields, and the error-covariance matrices have not yet been estimated. Since the structure functions of the vertical cloud profile are not known, the structure of the cloud background was retained, and only the CLW has been used as the cloud control variable. The element 22 of \mathbf{x} is set to CLW. As the radiative-transfer model needs a vertical cloud profile for simulating the radiances, the forward operator $\mathbf{y}(\mathbf{x})$ contains the rescaling of the cloud vertical structure by CLW. The liquid/(ice+liquid) ratio used in the ECMWF new cloud scheme is a simple quadratic function of the cloud temperature derived from Matveev (1984). The ice phase contained in the cloud was not taken into account in the retrieval process because the liquid absorption coefficient is 2 or 3 orders of magnitude larger than the ice absorption and because the volume scattering is not included in the radiative-transfer model (see section 4(a)). The retrieved CLW is, therefore, insensitive to the ice-water path of the background.

There are several reasons to expect large errors in the background CLW: there is a scale difference between the cloud represented in the ECMWF model and the cloud retrieved at SSM/I resolution, the time/space collocation between ECMWF fields and SSM/I observations is particularly critical because some clouds have a large spatial/time variability, and finally the cloud from the new cloud scheme has not been sufficiently validated. Therefore, the standard deviation of the CLW background has been set to 0.2 kg m^{-2} which represents a weak constraint. Note that CLW is a bounded control variable and that the Gaussian error hypothesis is not valid close to the lower bound (set to zero).

(iii) *Surface conditions.* The ocean surface contribution to SSM/I radiances depends on the sea surface temperature (SST) and on the sea surface roughness which can be related to the surface wind speed and direction.

The ECMWF SST has been used as a parameter in the radiative-transfer model, but was not included in the control variable as its error is around 1.5 K only.

The wind speed has been included in the control variable as element 21. An error in background wind speed of 2 m s^{-1} has been assumed following the results of Stoffelen and Anderson (1994). The sensitivity of SSM/I brightness temperature to wind direction is small, with a maximum signal of the order of $3 \times 10^{-2} \text{ K}$ per degree (see section 4(b)). The standard deviation of the ECMWF wind direction FG error (Stoffelen and Anderson 1994) is believed to be around 20° which is equivalent to a signal of 0.6 K in SSM/I brightness temperature. In order to exploit such a tiny signal in the retrieval, the forward model of the sea surface emissivity/scattering needs to be carefully validated and calibrated with a similar resolution. Since this is not the case for the sea-surface model used in the present study, the wind direction has not been included in the control variable, but was used as a parameter in the forward operator. This is equivalent to assigning a zero error to the background wind direction. The cross-correlation between the background errors in humidity, WS and CLW have been set to zero.

Although this paper presents retrievals above the ocean only, the 1DVAR scheme could be extended to land surfaces (bare soils, vegetation, ice, snow). A possible solution could be to use a simple land emissivity model with a limited number of parameters (see Grody (1988) for instance), and to include these parameters in the control variable \mathbf{x} . Equation (7) could then be used to assess the expected accuracies of the retrieval over land surfaces for different models ($\mathbf{y}(\mathbf{x})$) and errors (\mathbf{F} and \mathbf{B}) hypotheses.

4. RADIATIVE TRANSFER AND CALIBRATION

The radiative-transfer model (forward operator) maps the control variable \mathbf{x} into the radiance space and thus it is the heart of a variational retrieval system. The radiative-transfer model has to represent as accurately as possible the a priori knowledge of the

radiative properties of the atmosphere and of the surface. The modelling of the atmospheric contribution to the radiances is presented in 4(a). The sea-surface interaction with the radiation is described in 4(b). The correction of systematic errors in the radiative-transfer model and the model assumed for random errors (**F** matrix) are presented in 4(c).

(a) Atmospheric contribution

The radiative-transfer model used in this study is based on that of Phalippou (1991) but is restricted to the hypothesis of a non-scattering plane parallel atmosphere (Phalippou 1993). Only the key points of the model are reported below.

In order to solve the radiative-transfer equation in the atmosphere, a vertical discretization of the atmosphere is necessary. In this study, the atmosphere is described along the vertical by the pressure, temperature, specific humidity and cloud liquid-water density on the 31 ECMWF model levels, i.e. between the surface and the top of the atmosphere, which is about 10 hPa. This discretization of the atmosphere has been found adequate for modelling SSM/I radiances since the vertical resolution of the instrument is coarser than the spacing between two adjacent ECMWF model levels. No extrapolation of the atmospheric profile above 10 hPa has been necessary because the radiation absorption by atmospheric gases is negligible above that level for SSM/I frequencies. Each atmospheric layer defined by two adjacent model levels has been supposed homogeneous. The layer temperature and the layer absorption coefficient have been computed as the mean of the level values. The transmittance of the layer τ_i defined by levels i and $i - 1$ can then be written as:

$$\tau_i = \exp\{-(\alpha_{\text{gas}}(i) + \alpha_{\text{cloud}}(i)) \sec\theta \, dz_i\} \quad (10)$$

where α_{gas} and α_{cloud} are the gas and cloud absorption coefficients of the layer i , dz_i is the thickness of the layer computed using the hydrostatic equation, and θ is the local incidence angle. Note that SSM/I radiances have been simulated at the centre frequency of the channels and no spectral integration over the bandwidth has been done (i.e. a monochromatic assumption).

Oxygen and water vapour are the two main atmospheric gases absorbed in the microwave spectrum. A line-by-line model, including all the O_2 and H_2O absorption lines lying in the 1–1000 GHz band, is regularly updated by Liebe. The 1989 version (Liebe 1989) has been used in this study and will be hereafter referred to as the Liebe 89 model. At SSM/I frequencies, the major sources of uncertainties in the absorption coefficient are due to the errors in the H_2O line strengths and in the modelling of the so-called water vapour continuum. Although reports in the literature indicate that the versions before 1991 underestimated the absorption around the 22.235 GHz water vapour line (Westwater *et al.* 1990; Walter 1992; Keihm 1992) and that a similar tendency exists at 89 and 157 GHz (English *et al.* 1994), no attempt has been made to correct the water vapour absorption of the Liebe model in this study. The bias which might occur from the use of any absorption model is expected to be corrected by the global-bias correction scheme presented in section 4(c).

For the clouds, liquid-water absorption alone has been considered in this study, because of the uncertainties and complexity of radiative-transfer modelling in scattering atmospheres. The FOVs affected by volume scattering due to rain or appreciable amounts of ice-cloud have been detected at the pre-processing stage and after minimization (see section 5(c)). The cloud absorption is calculated using the Rayleigh approximation which is valid for the liquid-droplet spectrum of most non-precipitating clouds at SSM/I frequencies. It can be shown that under the Rayleigh approximation the cloud-absorption coefficient depends only on the complex dielectric constant, frequency, and liquid-water content (Ulaby *et al.* 1981). The dielectric constant of pure liquid water is computed using

the model reported by Ulaby *et al.* (1986) which is a function of frequency and temperature. The liquid water is assumed to be at the air temperature.

The full Planck function is used for computing the radiances, but the radiative-transfer model returns the vector y set to the brightness temperatures. The cosmic background radiation is set to 2.7 K.

(b) *Sea-surface contribution*

The atmospheric transmittances at SSM/I frequencies are large—around 70 to 90% in clear sky—so SSM/I observations are sensitive to the sea-surface parameters. The sea surface interacts with the radiation through direct emission and through the scattering of the downwelling atmospheric radiation. At SSM/I frequencies, the emission and scattering properties of the sea surface are mainly controlled by the wind and by the SST. The wind affects the sea-surface roughness and the sea-foam fractional cover. The dielectric properties and the emitted radiances of the sea depend on the SST.

The sea model used in this study is split in two parts: the foam-free sea model and the foam model itself.

(i) *Foam-free sea model.* It seems now established that in model–observation comparisons of the sea-surface emissivity the so-called two-scale models give better results than the geometrical optics (GO) models, particularly for frequencies below 20 GHz. However, the two-scale models are not suitable for fast modelling because of their complexity and related large computation time. On the other hand, Hollinger (1971) and Wilheit (1979) demonstrated that the GO models are a good approximation of the emission/scattering by a rough sea surface for incidence angles around 50° . More recently, Kunkee and Gasiewski (1994) and Guillou (1994) reported that the GO model was adequate for simulating the sea-surface radiative properties around 90 GHz. Therefore, a GO model of the sea surface has been used in this study.

The foam-free sea model is based on the GO approximation of scattering by a rough surface (Stogryn 1967; Wilheit 1979; Prigent and Abba 1990). The basic idea of the GO model is to represent the sea surface as a collection of flat facets, each one acting as a specular surface element. Each facet is described by its slope components along and across the wind direction. The Cox and Munk (1954) bidimensional slope distribution has been used in this study. The shape of this distribution is nearly Gaussian, with slope variances (cross wind and up/down wind) linearly related to the wind speed. A Gram Charlier series is used to modify a pure Gaussian distribution for accounting for the upwind/downwind asymmetry. As recommended by Hollinger (1971) and Wilheit (1979), only a fraction of the Cox and Munk slope variances has been taken for the SSM/I frequencies below 37 GHz.

The contribution of one facet to the upwelling radiation at sea level can be written as:

$$W(\mathbf{F}, d)[(1 - \Gamma(\mathbf{k}_0, \mathbf{F}, p))B(T_s) + \Gamma(\mathbf{k}_0, \mathbf{F}, p)R_{dn}(\mathbf{k}_0, \mathbf{F})] \quad (11)$$

with the geometry given in Fig. 2, where: $W(\mathbf{F}, d)$ is the weighting function of the facet, \mathbf{k}_0 is the observation direction, \mathbf{k} is the specular direction, \mathbf{F} is the vector perpendicular to the wave facet, p is the polarization (H or V), the incident plane being defined as containing the normal to an imaginary flat sea surface, d is the slope probability (Cox and Munk 1954), $\Gamma(\mathbf{k}_0, \mathbf{F}, p)$ is the facet specular reflectivity in V or H polarization, $R_{dn}(\mathbf{k}_0, \mathbf{F})$ is the downwelling radiance along the reflected specular direction \mathbf{k} , and $B(T_s)$ is the Planck function for the sea surface temperature T_s .

The first term in (11) is the radiance emitted by the facet and the second term is the radiance reflected after specular reflection. The radiance of the foam-free sea surface at

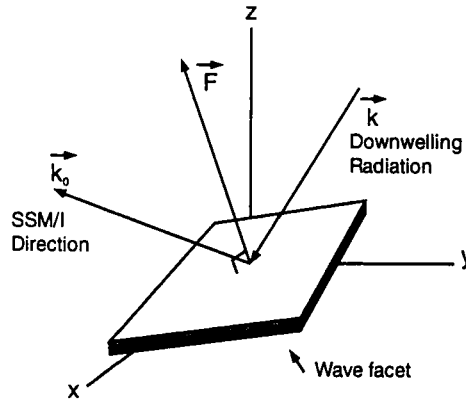


Figure 2. Geometry for the geometrical-optics model of the sea surface emission/scattering (see text for explanation of symbols).

the sea level R_{rough} is then obtained by integrating (11) over the upper hemisphere (uh):

$$R_{\text{rough}} = \int_{\text{uh}} W(1 - \Gamma)B(T_s) d\Omega + \int_{\text{uh}} W\Gamma R_{\text{dn}} d\Omega \quad (12)$$

where $d\Omega$ is the solid angle element and, for clarity, we have omitted the variable dependencies. The weighting function W must obviously satisfy the normalization relation:

$$\int_{\text{uh}} W d\Omega = 1. \quad (13)$$

Inserting (13) into (12) leads to:

$$R_{\text{rough}} = \left(1 - \int_{\text{uh}} W\Gamma\right)B(T_s) d\Omega + \int_{\text{uh}} W\Gamma R_{\text{dn}} d\Omega \quad (14)$$

where $(1 - \int_{\text{uh}} W\Gamma)$ is by definition the emissivity of the sea, and the second term of (14) is the scattered contribution. This equation shows that the contribution of the sea surface due to scattering cannot be simply written as the product of the surface reflectivity by the downwelling radiation along only one direction, as it is done for a specular surface.

The integrals in (14) are computed using discrete summations over an integration domain spanned by ± 2.5 times the standard deviations of the slope distribution. The facets which are not directly viewable from the satellite (i.e. $\cos(\mathbf{k}_0, \mathbf{F}) < 0$) are not taken into account in the summation (shadowing effect). We checked that, for the SSM/I geometry and wind speed less than 20 m s^{-1} , the number of hidden facets was negligible (less than 1%). When the downwelling radiation $R_{\text{dn}}(\mathbf{k}_0, \mathbf{F})$ comes from below the sea surface, then at least one additional reflection—hereafter referred to as multiple scattering—is happening. We have assumed that when a multiple scattering occurs then it is likely that the downwelling radiation incident on that facet is the result of a number of previous emission/reflections which create an unpolarized radiation.

The sensitivity of the radiances at the top of the atmosphere to multiple scattering is assessed by setting to its minimum and maximum possible values the radiation incident on a facet affected by multiple scattering. These values are respectively the downwelling radiance at nadir angle and $B(T_s)$. The variations of simulated 37 GHz radiances with wind direction are shown in Figs. 3(a) and 3(b) for the two hypotheses described above. In

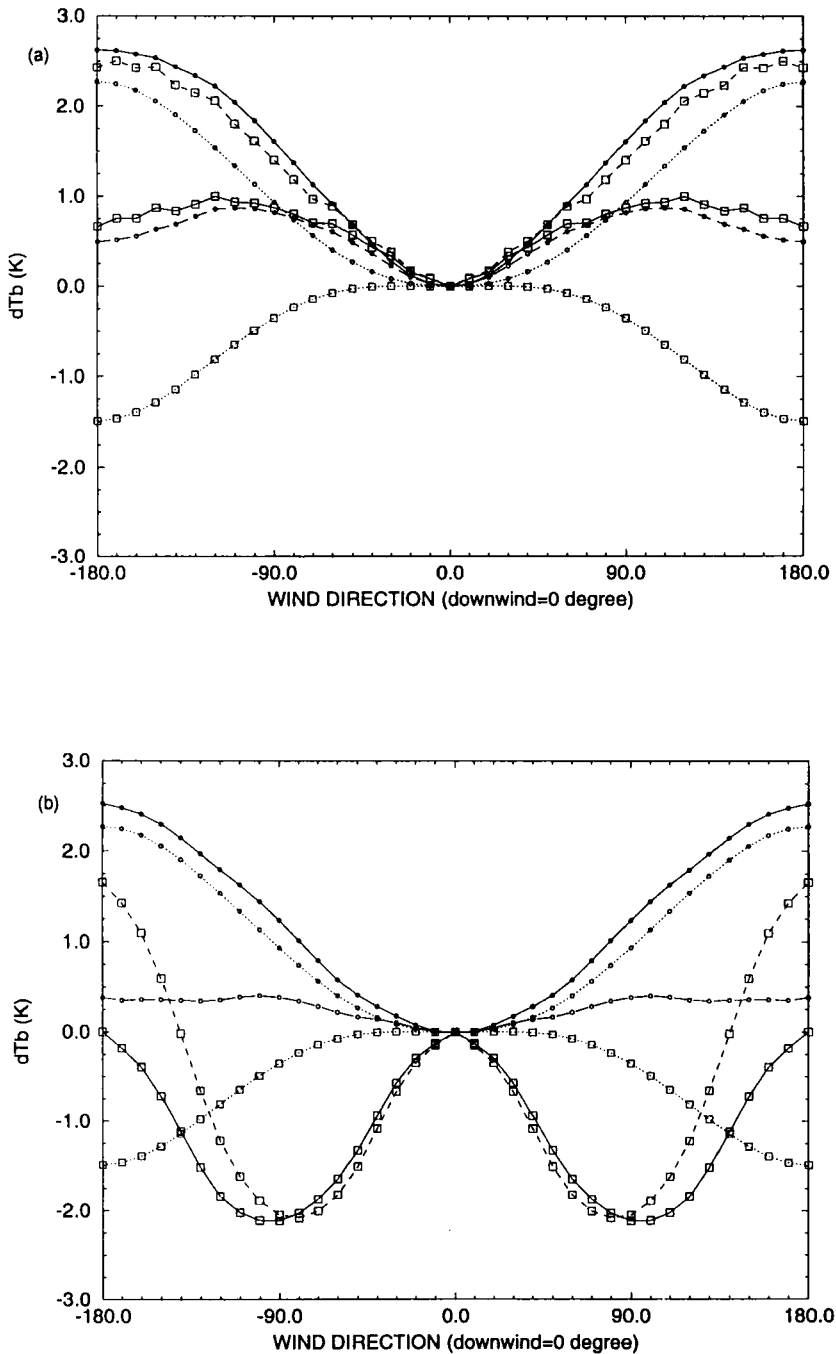


Figure 3. (a) Variation of 37 GHz brightness temperature (dT_b) as a function of wind direction for a 14 m s^{-1} wind speed. The downwelling radiation at nadir is used for multiple reflection (see text). The vertical and horizontal polarization are marked by dot and square symbols respectively. Dotted lines are for emission contribution, dashed lines are for scattering contribution, full line is for the total. Total precipitable water vapour = 14 kg m^{-2} , sea surface temperature = 290 K , no cloud. (b) As (a) except that $B(T_s)$ (Planck function of sea surface temperature) is used as the downwelling radiation for multiple reflection.

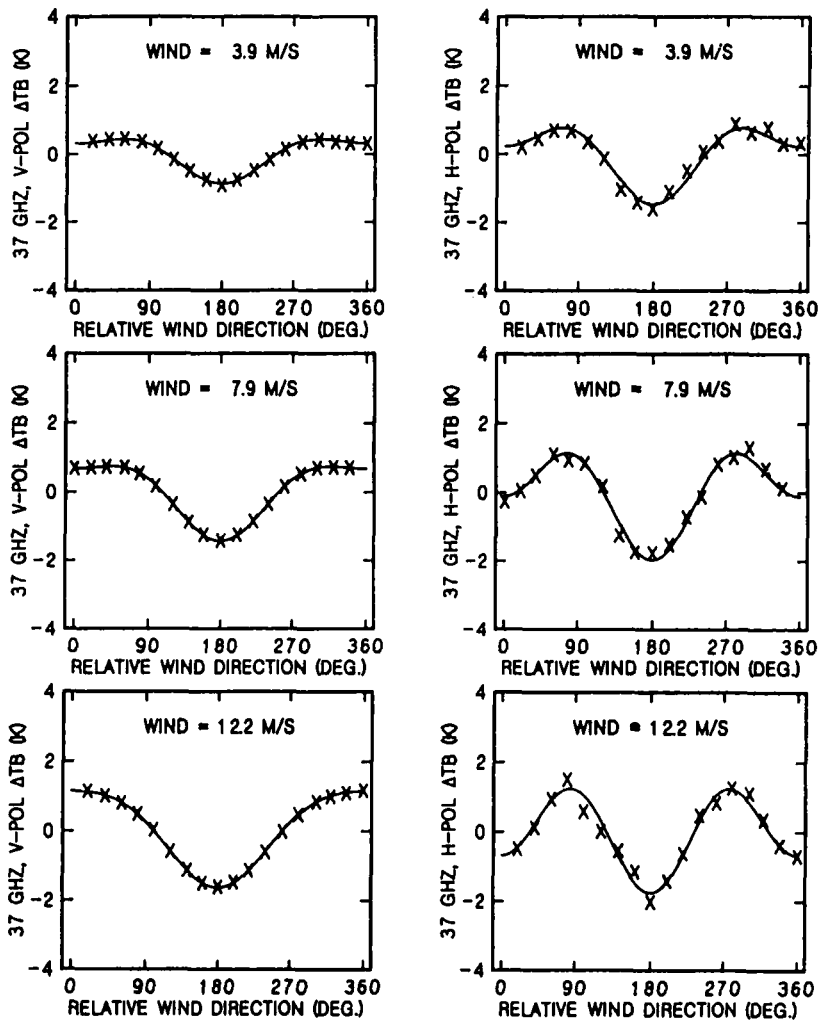


Figure 4. Wind direction signatures as observed with SSM/I at 37 GHz (from Wentz (1992)). Note that the downwind direction is shown as 180° (on these figures only).

both cases the GO model results are in surprisingly good agreement with the observations reported by Wentz (1992) (see Fig. 4) for the vertical polarization, although the amplitude of the signal is slightly bigger in the observations. However, Fig. 3(b) shows that the crosswind radiance in horizontal polarization is lower than the upwind or downwind radiance, which is the opposite of Wentz's findings but is in agreement with the simulations of Stogryn (1967). When the nadir downwelling radiation is taken for the facets affected by multiple scattering (Fig. 3(a)), then the variations of the simulated radiances are in phase with Wentz's results in V and H polarization and, therefore, this last hypothesis has been retained. Finally, from Fig. 4 the maximum sensitivity of the radiances to the wind direction can be estimated to be around 0.03 K per degree in V polarization and 0.04 K per degree in H polarization for a wind speed of 12 m s^{-1} . Once again the results of the GO model suggest lower sensitivities of the radiances to the wind direction than is reported in Fig. 4. Similar trends in the wind direction sensitivities were observed in our simulations for other SSM/I frequencies.

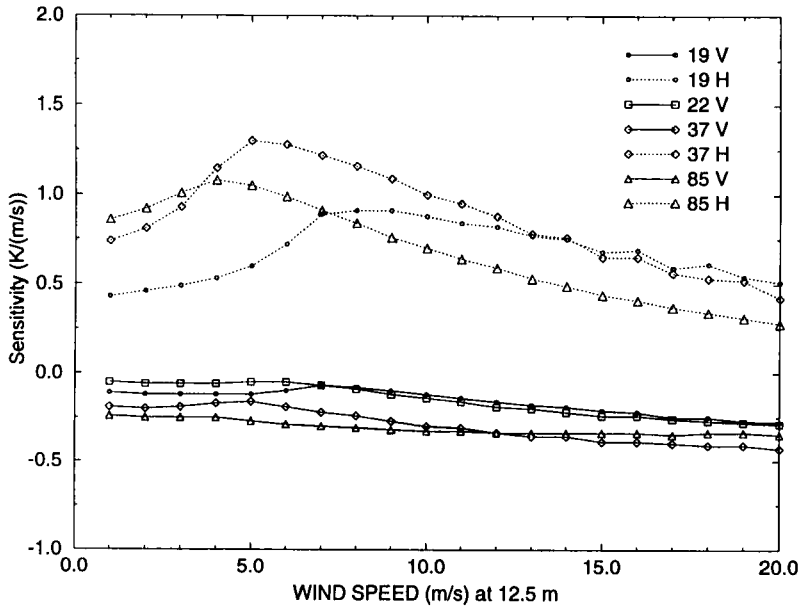


Figure 5. Sensitivity of brightness temperature to sea-surface roughness (foam-free) for downwind observation at 19, 22, 37 and 85 GHz for vertical (V) and horizontal (H) polarization. The modified Cox and Munk slope distribution (slope variances are frequency dependent) is used to relate the sea-surface roughness to wind. Total precipitable water vapour = 14 kg m^{-2} , sea surface temperature = 290 K , no cloud.

The sensitivities of radiance to wind speed for a foam-free sea are plotted in Fig. 5 for a downwind geometry. These curves show largest sensitivities in H polarizations with maxima located between 4 and 6 m s^{-1} .

In summary, the GO model is capable of reproducing the wind direction signal which has been observed by microwave radiometers at 19 and 37 GHz. In the model, this signal comes from the anisotropy of the slope distribution. The upwind/downwind signal observed in V polarization is particularly well reproduced by the GO model. The treatment of multiple reflections is a key point for modelling of the wind direction signal in H polarization. As mentioned in section 3, the wind direction from the ECMWF FG has been used as a parameter of the radiative transfer, but the wind direction was not modified during the iterative retrieval.

(ii) *Sea-foam model.* Sea foam is a mixture of air and water which is known to increase the sea emissivity in V and H polarization. The results reported by Stogryn (1972) and Smith (1988) show that the effect of sea foam on the apparent radiance of the sea cannot be ignored at SSM/I frequencies. Although the sea foam is an inhomogeneous medium, we have made the usual assumption that the foam contribution to the sea surface apparent radiance can be described by the fractional foam cover C_f and by the foam emissivity. The sea surface radiance at the sea level R_{sea} is given by the linear combination of the foam-free sea radiance and the sea-foam radiance alone R_{foam} :

$$R_{\text{sea}} = (1 - C_f)R_{\text{rough}} + C_f R_{\text{foam}}. \quad (15)$$

The fractional foam cover has been computed as an exponential function of the wind speed following Monahan and O'Muircheartaigh (1980). As pointed out by Petty (1990) there is no evidence that this fractional cover derived from optical measurements represents the

effective fractional cover in the microwave band. It will be shown later that the sea-surface model including roughness and foam must be tuned anyway, in a rather crude way, against the observations.

Very few attempts have been made to measure the sea-foam radiative properties. Smith (1988) derived sea-foam emissivities from airborne radiometer measurements at 19 and 37 GHz, and reports that the sea-foam emissivity model of Stogryn (1972) is in good agreement with his observations. The Stogryn model has been used in this study to assess the sensitivity of SSM/I radiances to sea foam. The simulated radiance sensitivities to wind speed, including surface roughness and sea foam, are given in Figs. 6(a) and 6(b) for an upwind and downwind configuration. These curves show that the sensitivities to wind speed generally increase with wind speed except for the 85 GHz H polarized channel. The radiance sensitivities to wind speed in V polarization are much lower than in H polarization. Comparisons between Fig. 5 and Figs. 6(a) and 6(b) indicate that the sea foam has a significant effect on the radiance sensitivities for wind speed as low as 7 m s^{-1} as previously reported by Wilheit (1979). The signature of the wind direction due to the anisotropy of the surface roughness remains visible when the sea foam is included in the sea-surface model.

(iii) *Sea-surface model tuning.* When the Stogryn sea-foam emissivity model was used in the retrieval method presented in section 2, several problems were found for moderate and high wind speeds (above 10 m s^{-1}). The retrieved wind speed had a tendency to be systematically too strong (the field of the difference between retrieved and background wind speed was positively biased), the fit to the radiances was poor and the field of the differences between the observed and measured V and H radiance differences had a strong wind-speed signature. These diagnostics indicated a problem with the sea-surface model. The sea-foam modelling was first suspected, as its role is crucial at high wind speeds. The polarization problem mentioned above suggested that the mixing of the polarization due to wind speed was globally (roughness+foam) too weak. A simple test was then done by setting the sea-foam emissivity to unity regardless of frequency and polarization. The results immediately improved for all the aspects. It must be pointed out that although this empirical tuning against the radiances and the background is done through a correction on the sea-foam emissivity alone, it represents an overall simple tuning of the complete sea modelling (roughness+foam). The sensitivity of SSM/I radiances to wind speed are plotted in Fig. 7 for a sea-foam emissivity equal to 1. Comparisons with Fig. 6(b) show the large differences between the Stogryn sea-foam model and the black-body assumption in particular in H polarization. The highly nonlinear shape of the curves for wind speed above 10 m s^{-1} are due to the power law used for the foam cover. The impact of the sea-surface modelling on the theoretical retrieved wind-speed accuracy is discussed in section 5.

(c) *Observation errors and forward-operator errors*

The diagonal terms of the observation covariance-error matrix \mathbf{O} (see (1)) are set to the radiometric sensitivities of SSM/I (Hollinger *et al.* 1990). These sensitivities were estimated for the SSM/I instrument on board the F-8 satellite, and we have assumed that they are representative of the F-11 data which have been used in this study. The observation errors have been assumed uncorrelated, i.e. the \mathbf{O} matrix is diagonal. In any case SSM/I radiometric sensitivities are not the driving factor in the error budget because they are much lower (typically 0.6 K) than the errors we have assumed in the forward model.

The errors of the forward model (\mathbf{F} matrix) are difficult to evaluate objectively as they would require the comparison between microwave observations and radiances simulated from collocated accurate measurements of the atmospheric profile and sea-surface

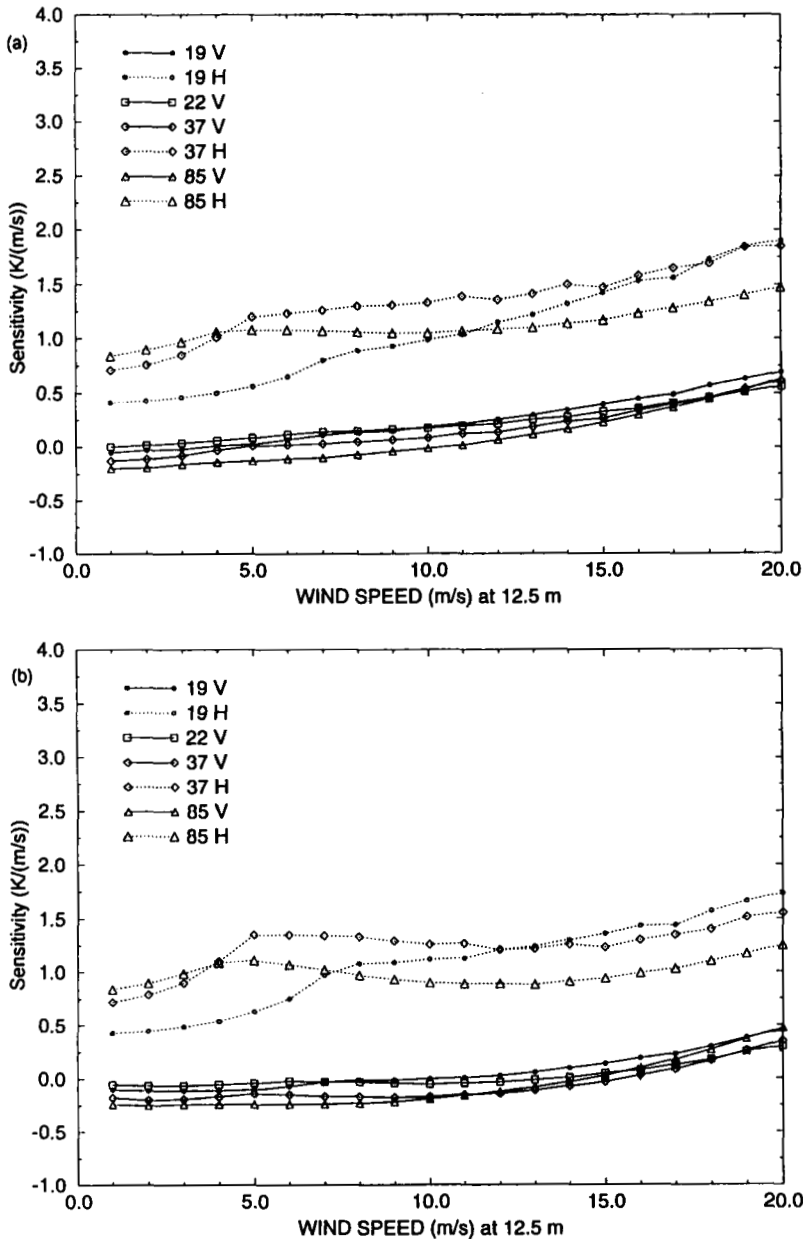


Figure 6. Sensitivity of brightness temperature to wind speed for (a) upwind and (b) downwind observations, including the surface roughness and the Stogryn (1972) sea-foam model, at 19, 22, 37 and 85 GHz for vertical (V) and horizontal (H) polarization. Total precipitable water vapour = 14 kg m^{-2} , sea surface temperature = 290 K, no cloud.

conditions. We have assumed that the forward-model errors were uncorrelated. Note that this hypothesis is probably very crude, in particular for the V and H channels at the same frequency. The $\mathbf{F} + \mathbf{O}$ matrix is thus diagonal and the square roots of its diagonal terms have been set to 2 K for the 19, 22 and 37 GHz channels and 3 K for the 85 GHz channels. Although these values are subjectively specified, we have verified that the a posteriori variances given by the diagonal terms of (7) are consistent with previous estimates of the

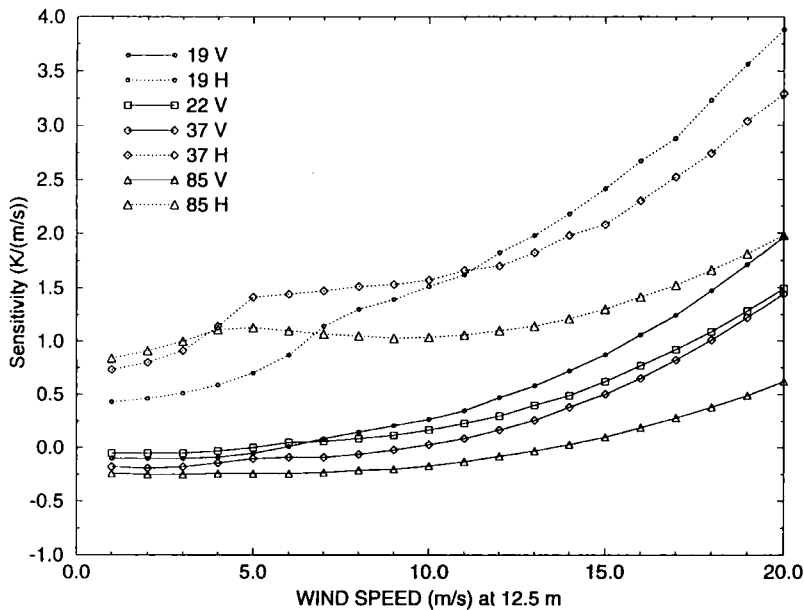


Figure 7. As Fig. 6(b) but the sea foam is assumed to be a black body at the sea surface temperature.

accuracy of the retrieved parameters, as reported in the literature (see section 5). Similar error values are also reported by (Petty 1990) for his SSM/I forward model. The larger errors at 85 GHz are supposed to account for the difference between the FOV of the lowest frequency channels and the 85 GHz FOV.

Since the ECMWF fields are assumed to be globally unbiased, the mean differences over a large number of cases between observed and simulated radiances are expected to be zero at the end of the minimization for each channel. If this is not the case, then a bias exists in the radiances or in the forward model or in both. Ideally a bias correction scheme must process a large number of data to be statistically representative, and the quality control must be efficient to ensure that the radiative processes which are not represented by the forward model are screened out (scattering by cloud or rain for instance in this case). These conditions were not met in this study and a very simple iterative estimation of the biases has been done by processing several SSM/I scenes and using the estimated biases from the previous scene as an input for the current scene. This procedure has been repeated until a reasonable convergence (around 0.5 K) was reached. The 'final' estimated brightness-temperature biases (to be added to the measurements) are reported in Table 2. For a few independent scenes (i.e. scenes which were not used in the bias estimation), we have checked that there is no large bias in brightness temperatures at the end of the retrieval if the above corrections are made before the inversion.

TABLE 2. BIAS CORRECTION (TO BE ADDED TO THE OBSERVED BRIGHTNESS TEMPERATURES) IN THE VERTICAL (V) AND HORIZONTAL (H) POLARIZATIONS

Frequency/Polarization (GHz)	19V	19H	22V	37V	37H	85V	85H
Bias (K)	-2.35	-2.25	0.25	0	0	1.8	1.8

5. RESULTS AND DISCUSSION

The variational method presented in section 2 involves the simulated SSM/I radiances and their derivatives with respect to the control variable, i.e. the Jacobian matrix \mathbf{K} . In this study \mathbf{K} is computed using a forward finite-difference method, which is expensive as it requires two runs of the forward model for each frequency and for each control variable at every iteration of the minimization. Moreover the radiative-transfer model itself is particularly slow as it uses a line-by-line computation of the atmospheric gas transmittance and the sea-surface model described in section 4. For these reasons, the 1DVAR method presented in this paper has only been applied to a limited number of SSM/I orbits. Its application to operational data assimilation or any quasi real-time processing will require the use of a fast radiative-transfer model, such as the one described by Eyre (1991) for the atmospheric part, the development of a fast model for the sea-surface model, and the implementation of the adjoint technique (Talagrand 1988).

The results presented in this section are for an ascending SSM/I (F-11 satellite) pass between 60°S and 60°N for 4 January 1994. The ascending local crossing time is 17:04. The land areas represented in white in Figs. 8–11 are Africa, the coasts of Spain, Ireland and Iceland. This scene includes a large variation in the meteorological parameters of interest for this study. Figures 8(a), 10(a) and 11(a) show that the background (i.e. ECMWF fields) total precipitable water vapour varies between 5 and 60 kg m⁻², WS between 0 and 20 m s⁻¹ and CLW between 0 and more than 0.4 kg m⁻². The highest WS and CLW are associated with a frontal system in the Atlantic. The retrieved humidity fields, the wind field and CLW are presented and analysed in the subsections 5(a) to 5(c).

The 1DVAR retrievals are performed for the so-called A scans (Hollinger *et al.* 1990) which contains the low-frequency channels (19 to 37 GHz) and the high-frequency channels (85 GHz). A 2 × 2 undersampling along and across the A scans is taken to reduce the computation time. Therefore, the fields presented in the following have a sampling of 50/50 km.

(a) Humidity fields

Although the 3D humidity fields are retrieved, the results are presented as total precipitable water vapour for convenience. Figures 8(a) and 8(b) show the background TPW and TPW retrieved with the present method. The TPW retrieved with the method of Alishouse *et al.* (1990), hereafter referred to as Alishouse TPW, is used as an independent ‘ground truth’ as the oceanic radiosoundings are too sparse to provide useful comparison for a single scene. The Alishouse algorithm is based on the regression between TPW derived from radiosonde observation and SSM/I measurements. This regression was initially developed for SSM/I on board the F-8 satellite and we have assumed that it is valid for F-11 data. The errors of the Alishouse TPW estimates can be expected to be fairly uncorrelated with the TPW estimation errors of the present method as the only common source of random-error correlation between the two methods is due to the SSM/I measurement noise. The accuracy of the Alishouse TPW is of the order of 2 to 4 kg m⁻² depending on weather conditions. Alishouse TPW is shown in Fig. 8(c), where the black areas correspond to precipitation detection. As this screening might also reject non-precipitating heavy cloud in which we are interested, a 1DVAR retrieval is, however, attempted when rain is detected by the Alishouse test.

The comparison of Fig. 8(b) and 8(c) shows that the spatial horizontal structure of 1DVAR TPW agrees remarkably well with the Alishouse TPW field. The background TPW is very close to the 1DVAR TPW in the northern hemisphere. More differences between 1DVAR TPW and the background appear in the southern hemisphere even at large scale.

It is noticeable, for instance, that the humidity of the background is too large in the 10° to 30°S latitude band as confirmed by the 1DVAR and Alishouse retrieval. The fact that the gradients are sharper in the retrieved fields is probably due to the resolution of SSM/I which is around 50 km compared with about 125 km for the ECMWF (T106) model. It is noticeable that the 1DVAR provides reasonable TPW for the areas which are detected as rainy by Alishouse, suggesting that the present method is fairly robust in the presence of rain contamination.

The scatter plot (Fig. 12) shows a general good agreement between 1DVAR TPW and Alishouse TPW. The standard deviation of the difference between these two estimations is 1.4 kg m^{-2} . Overestimation and underestimation of Alishouse TPW at respectively low and high water vapour content are noticeable in Fig. 12. Such local biases have already been reported by Alishouse *et al.* (1990) and Petty (1990). They are due to the intrinsic nonlinearity of the retrieval problem which is difficult to handle when a regression-type method is used.

However, these results suggest that the regression technique provides accurate SSM/I TPW in almost all weather conditions, including those (clouds, high wind, large TPW) which might be suspected not to be well represented in the data set originally used by Alishouse to derive the regression coefficients. A possible explanation of this behaviour would take account of the quasi-linearity of SSM/I radiances with respect to TPW and the fact that the SSM/I radiances are 'mainly' sensitive to TPW. This last point is also confirmed by the results of Ruprecht *et al.* (1992) who performed a principal-component analysis of the covariance matrix of SSM/I brightness temperatures for the five lowest frequencies. Only two significant eigenvectors were found, explaining respectively 86% and 13% of the total variance. They found that the structure of the first eigenvector was very similar to the structure of the water vapour absorption coefficient and they concluded that this first eigenvector mainly described the variance of TPW. The second eigenvector was more difficult to interpret as it was found to be related to CLW or to WS depending on weather conditions.

The theoretical error in the retrieved humidity profiles is given by the **S** matrix (7). As the humidity control variable is the Napierian logarithm of the specific humidity, the elements of **S** are difficult to interpret as such. A more appropriate variable is the equivalent error in TPW space, which can be computed from each retrieved humidity profile and from the **S** matrix (the operator mapping the specific-humidity profile into TPW being simply the vector containing the atmospheric layer thicknesses). For the **B** matrix presented in section 3 the a priori background TPW errors vary between 2 and 19 kg m^{-2} for respectively a dry (5 kg m^{-2}) and a tropical (more than 50 kg m^{-2}) humidity profile. For the above conditions, the theoretical 1DVAR accuracy varies between 1 and 2 kg m^{-2} confirming once again the quality of SSM/I for oceanic humidity measurements.

In order to assess the humidity vertical profiling capability of the present retrieval method, the total precipitable water is computed for three layers, i.e. 300–500 hPa, 500–700 hPa and 700 hPa to surface pressure, for the background and the retrieved humidity profile. The normalized differences (defined as the difference between the retrieved and the background TPW divided by the background TPW) are shown in Fig. 9 for the three layers defined above. The comparison between these three pictures shows that the patterns are similar but that differences exist in some areas. This indicates that the retrieved humidity profile cannot be simply obtained by rescaling the background humidity profile. Two conclusions can be drawn. SSM/I measurements are sensitive to the humidity profile between 300 hPa and the surface, and do not only measure the low tropospheric water vapour. This is confirmed by the examination of the elements of the **K** matrix and by the normalized TPW differences shown above. The change in the structure of the humidity

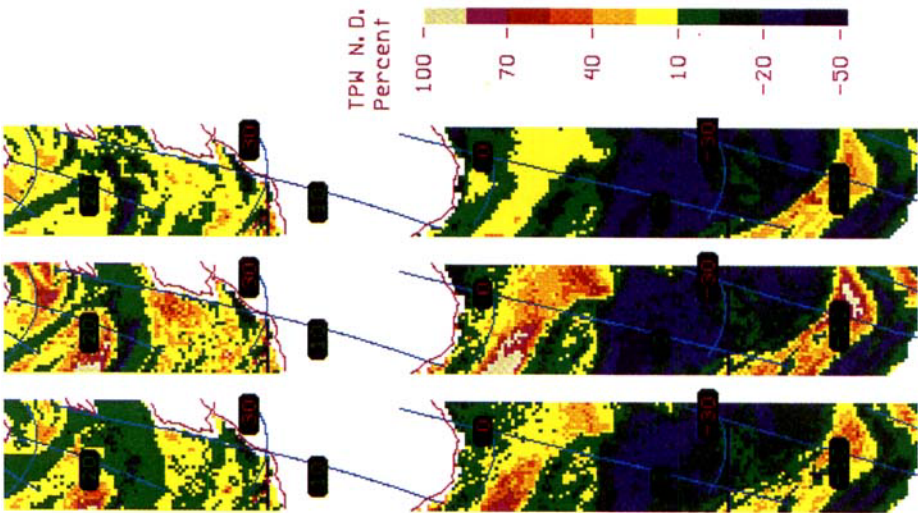


Figure 9. Normalized total precipitable water vapour differences, defined as (background - IDVAR)/background, for three layers. From left to right, 300-500 hPa, 500-700 hPa, and 700 hPa to surface pressure.

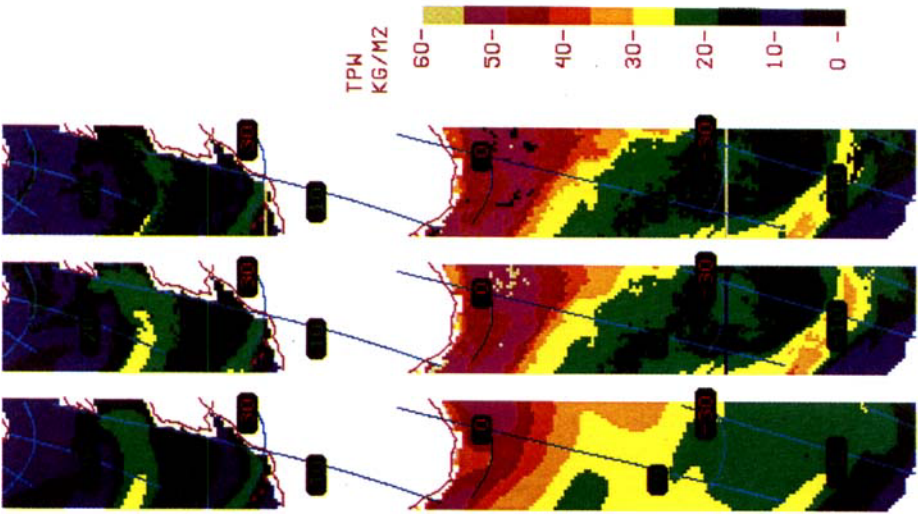


Figure 8. Total precipitable water vapour from, left to right, the background, IDVAR, and the Alishouse *et al.* (1990) algorithm.

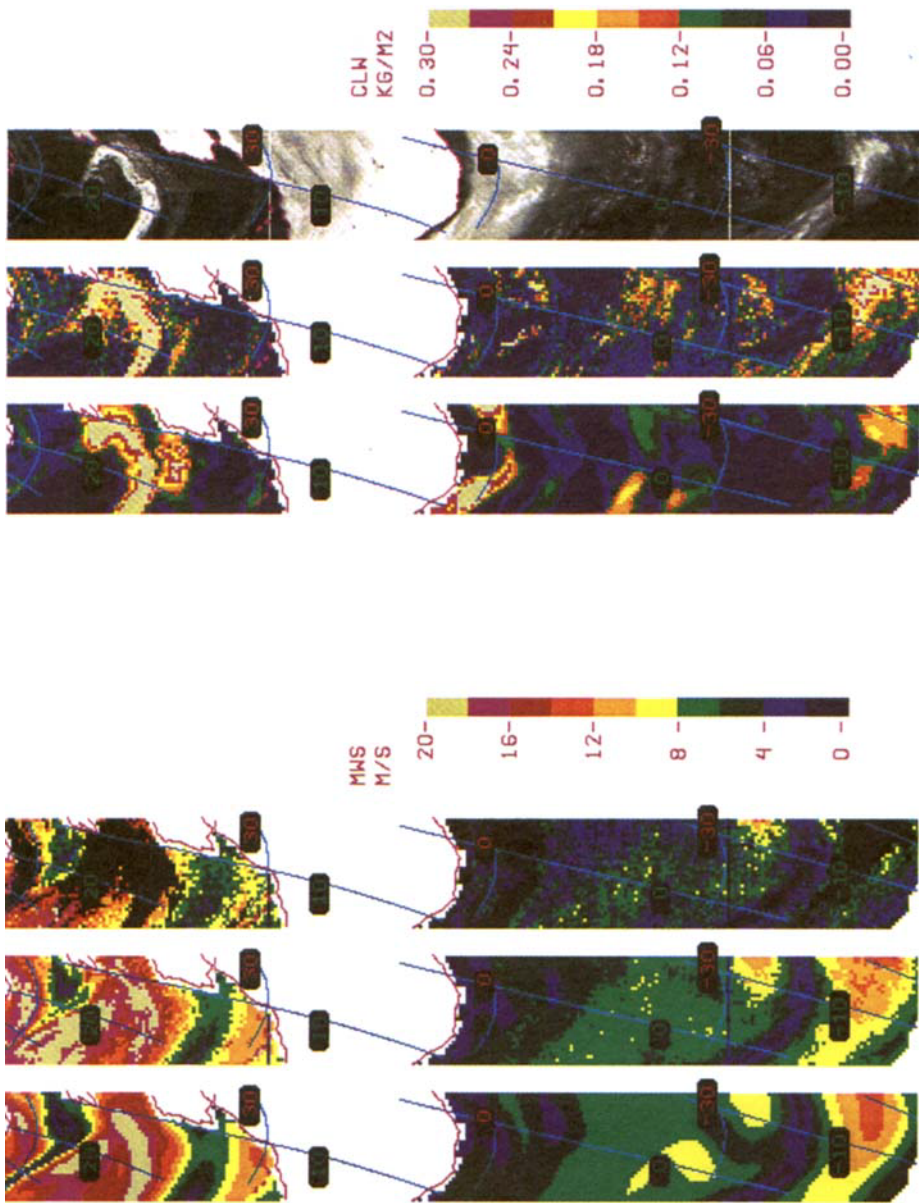


Figure 11. Cloud liquid-water content from, left to right, the background, IDVAR, and the 85 GHz SSM/I brightness temperature in horizontal polarization.

Figure 10. Marine wind speed at 10 m from, left to right, the background, IDVAR, and the Goodberlet *et al.* (1992) algorithm.

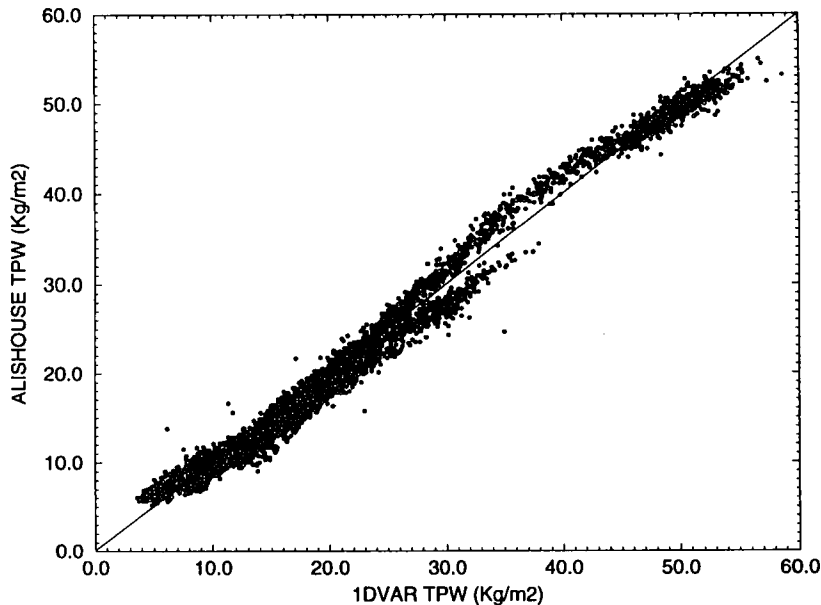


Figure 12. 1DVAR-retrieved total precipitable water vapour versus total precipitable water vapour retrieved using the method of Alishouse *et al.* (1990). (6400 points).

profile is mainly controlled by the covariance matrix of the first guess (**B**) and by the water vapour saturation constraint (\mathcal{F}_{sat}). Indeed, this constraint may strongly modify the humidity vertical structure as it creates a highly nonlinear effect (saturation).

(b) Wind-speed fields

Because of the lack of independent coincident wind-speed measurements over ocean, the wind speed derived from SSM/I using the Goodberlet *et al.* (1992) algorithm is used for qualitative comparison purposes only. The Goodberlet wind speed, originally retrieved at 19.5 m, has been extrapolated at 10 m assuming a neutral stability condition. The background, the 1DVAR and the Goodberlet wind-speed fields are shown in Fig. 10. The Goodberlet wind speed is not plotted (black areas in Fig. 10(c)) when its accuracy is less than 2 m s^{-1} according to the accuracy flag system used by Goodberlet *et al.* (1992). This screening eliminates most of the frontal areas in the Atlantic where the higher wind speeds occurred.

The comparison between the three wind fields shows a good overall agreement. The fact that the 1DVAR retrieved wind field is smoother than the Goodberlet wind field is due to the background constraint. It is in particular noticeable that the 1DVAR wind speed differs only slightly from the background. One might expect such a result because of the strong but objective constraint (2 m s^{-1}) imposed by the background term. No significant change has been observed in the 1DVAR retrieved wind field when a 3 m s^{-1} background wind-speed error was used. On the other hand, we have seen in section 4 that the sensitivity to the wind speed was large for moderate and high wind speed. As no particular unreasonable feature appears in the 1DVAR retrieved wind field, it could be assumed that the sea model is satisfactory for inverting SSM/I radiances. However, it is particularly difficult to demonstrate that the accuracy of the retrieved wind field is better than the accuracy of the background, i.e. that there is an improvement on the wind

speed a priori knowledge. This would need a comparison with collocated independent and accurate wind-speed measurements. This validation work is beyond the scope of this study, and we have simply calculated the theoretical 1DVAR wind-speed accuracy using (7). This accuracy depends mainly on wind speed and to a smaller extent on the other parameters as suggested by the nonlinearity of the radiance sensitivities with respect to wind speed. The typical value of the 1DVAR retrieved wind-speed accuracy is around 1.5 m s^{-1} for wind speeds lower than 12 m s^{-1} . This value is equivalent to the accuracy which would result from a minimum variance estimator using a background error of 2 m s^{-1} and an independent wind-speed measurement with a 2.3 m s^{-1} accuracy. For higher wind speeds, the retrieved wind-speed error decreases dramatically to a surprising 0.5 m s^{-1} for a wind speed of 20 m s^{-1} . This theoretical accuracy is believed to be very optimistic and is due to the crude approximation used for the sea-foam emissivity (see section 4). When the Stogryn sea-foam model is used the wind-speed accuracy at 20 m s^{-1} is a more realistic 1.3 m s^{-1} . As already outlined in section 4, the modelling of the sea foam is, therefore, a key point for the modelling of the sea-surface emission for wind speed above 10 m s^{-1} .

Finally, we must emphasize the advantage of having a good quality wind-speed background for the inversion, in particular for the retrieval of wind and CLW. For certain conditions the wind speed and the cloud have similar effects on the radiances (depolarization effect, increasing of radiances in H polarization). In these conditions the inversion problem is particularly ill-conditioned if no a priori information is available, and a cloud signature can easily be interpreted as a wind-speed effect and vice-versa. This problem affects most of the SSM/I regression algorithms which are used for retrieving separately WS and CLW. This effect is visible for instance in Fig. 10(c) where the speckle is believed to be due to cloud contamination. In the present method, when a cloud–wind ambiguity arises, the minimization will prefer to modify the CLW as the constraint on that parameter is weak compared with the wind-speed constraint. This will give a chance to the algorithm to move away from the initial ambiguous solution. However, the drawback is that in case of gross error in the background wind speed, due for instance to the mis-location of a frontal system, the wind constraint can be too strong and not appropriate.

(c) *Cloud liquid-water path*

The background and the 1DVAR retrieved CLW are shown in Fig. 11. Because of the complete lack of ground truth for the CLW and the large uncertainties existing in the available regression algorithms, the 85 GHz H polarized brightness temperature is used as cloud imagery. This SSM/I channel is sensitive enough to the cloud for identifying the moderate to heavy cloud patterns as shown in Fig. 11(c).

The position of the clouds and the CLW of the ECMWF background agree reasonably well with the 1DVAR retrieved cloud fields for the frontal system in the North Atlantic. More discrepancies can be observed in the southern hemisphere, in particular in the tropical and subtropical areas. The large differences between the background and the retrieved CLW occurring between 20° and 30°S are associated with a background TPW overestimation. The visual comparison between Figs. 11(b) and 11(c) shows that the retrieved CLW is correlated with the 85 GHz H polarized brightness temperature, as one might expect as this channel is used in the retrieval process. Note that the problem of negative values of the retrieved CLW which appear in regression-based retrievals, is avoided here thanks to the positivity constraint used during the minimization (see section 2).

The retrieved CLW varies between 0 and 0.4 kg m^{-2} . This last value is believed to be around the maximum CLW which can be retrieved with the present method. Indeed, above that value, ice particles or/and rain are likely to occur in large amounts producing a significant scattering of the radiation. The detection of such events can be done, before

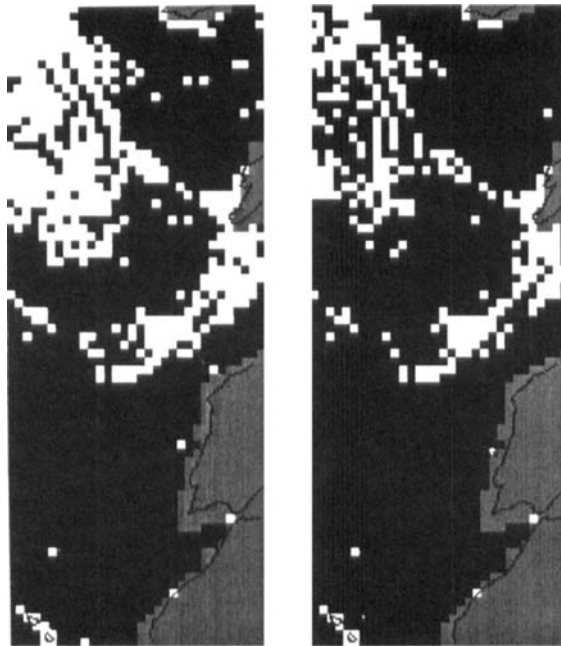


Figure 13. Scattering detection (white areas) using the observation cost function (left), and using the Ferraro *et al.* (1994) algorithm (right) (see text).

attempting the inversion at the pre-processing stage, by using the so-called scattering-index method described by Grody (1991) and Ferraro *et al.* (1994), and after the inversion by applying a threshold on the acceptable observation cost function \mathcal{J}_o . In the last case, the retrieval will be rejected when the radiances are not consistent with each other and the a priori information. Obviously precipitation might occur without being detected by the pre-processing and, therefore, degrade the quality of the retrieval. For instance, in the absence of scattering (small liquid rain drops), it is likely that the rain signature will be interpreted as cloud liquid-water because the spectrum of the rain absorption is identical to the spectrum of the cloud absorption in the Rayleigh approximation limits. In order to compare the scattering-index method and the scattering detection using the observation cost function, 1DVAR retrievals have been performed even when volume scattering was detected at the pre-processing stage. The areas for which the observation cost function is greater than 3.5 are plotted in Fig. 13(a). For comparison, the areas detected as rainy by Ferraro *et al.* are shown in Fig. 13(b). Data from the northern hemisphere alone are shown in Fig. 13 because no rain (or more generally volume scattering) occurrence was detected in the rest of the scene. The 3.5 threshold is the value that the observation cost function would have at the end of the minimization if the departure between measured and computed radiance was equal to the error standard deviation (diagonal elements of $\mathbf{O} + \mathbf{F}$) for each channel. The two methods of rain detection give similar patterns, showing that the quality control of the 1DVAR retrieval can be done as a post-processing based on the value of the cost function for instance. In both cases, rain is detected in the core of the frontal system occurring in the Atlantic. The post-frontal area which is detected as rainy presents very extreme conditions, i.e. low total precipitable water (6 kg m^{-2}), strong wind speed (20 m s^{-1}), very cold surface temperature (277 K) and air temperature (below 273 K) and probably an inhomogeneous cloud field as suggested by the 85 GHz brightness temperature (Fig. 11(c)). Therefore, the fact that this area is detected by 1DVAR as rainy

can also be explained by some deficiencies in the forward model (sea dielectric constant, gas absorption, sea modelling, etc.) which may be inadequate in such extreme conditions. The detection of rain by the scattering-index method for the same area is reassuring, although this method might also be questionable for these extreme conditions.

The CLW theoretical accuracy derived from (7) is typically equal to 0.02 kg m^{-2} for low to moderate CLW, i.e. between 0.01 and 0.4 kg m^{-2} . However, for high wind speed (i.e. above 15 m s^{-1}) the error increases dramatically and can reach 0.1 kg m^{-2} for a 20 m s^{-1} wind speed. This effect is due to the high sensitivity of the radiances to the wind speed above 10 m s^{-1} as outlined in the previous sections.

Two modifications of the cloud background described in section 3 have been made for testing the sensitivity of the 1DVAR retrieval. The first one was to increase the CLW background standard error from 0.2 to 0.5 kg m^{-2} . The results showed that the retrieved TPW, WS and CLW were not significantly dependent on this parameter. The second change was to use a cloud background profile derived from the humidity and the temperature background profile in a very simple way: the cloud water density was set to 0.1 g m^{-3} for each level having a relative humidity greater than 70% and a temperature above 253 K. This 'new' background cloud field was significantly different from the original background cloud field. However, the 1DVAR retrieved CLW, using the new background cloud field and a 0.2 kg m^{-2} background CLW error, was very close to the original CLW shown in Fig. 11(b). This result suggests that the retrieval method is not very sensitive to the background CLW as long as the cloud is occurring at a vertical location which is consistent with the humidity and the temperature profile.

Finally, Table 3 gives the mean value and the standard deviation of the difference between observed and computed SSM/I radiances at the end of the minimization for the scene described above. The mean values are small for all channels. The standard deviations are of the order of 1 K for the low-frequency channels and 2 K for the 85 GHz channels, i.e. lower than the noise assumed in the measurements and in the forward model.

TABLE 3. OBSERVED MINUS COMPUTED BRIGHTNESS-TEMPERATURE STATISTICS AT THE END OF THE MINIMIZATION OF THE COST FUNCTION

Frequency (GHz)	Polarization	Minimum (K)	Maximum (K)	Mean (K)	Standard deviation (K)
19	Vertical	-3.77	8.92	0.15	0.94
19	Horizontal	-7.80	10.75	-0.36	1.04
22	Vertical	-3.97	4.48	0.52	1.08
37	Vertical	-3.32	7.53	-0.13	1.14
37	Horizontal	-5.08	10.27	0.21	1.01
85	Vertical	-20.07	7.05	-0.01	1.85
85	Horizontal	-20.06	15.84	0.12	2.11

These statistics have been computed for the scene presented in section 5. This scene has not been included in the estimation of the bias correction (see text).

6. SUMMARY AND CONCLUSIONS

A variational method is described in this paper for the simultaneous retrieval of the atmospheric humidity profile, wind speed and cloud liquid-water path from SSM/I observations. The method is based on the minimization of an objective cost function and is mathematically similar to the data-assimilation problem in NWP. The main purpose of

this study was to demonstrate the feasibility of the method with the present knowledge of radiative-transfer modelling and to show its potential for NWP.

The TPW field retrieved with 1DVAR compares well with Alishouse TPW. However, our results suggest that the Alishouse TPW exhibit local biases for low and high TPW values. The present method has two advantages for the retrieval of TPW. The approach is fully nonlinear and no approximation of the radiative transfer is needed; and the use of the humidity profile as a control variable, the use of a priori information and the control of supersaturation allow us to distribute the humidity increments in an optimal way. The theoretical accuracies of the 1DVAR TPW are estimated to lie between 1 and 2 kg m⁻² depending on weather conditions, representing an improvement of a factor of 2 to 8 on the ECMWF TPW error.

When TPW, WS and CLW are retrieved separately there might exist ambiguities in the retrieved products. For instance, cloud or TPW signatures can be interpreted by the regression as a wind-speed signal (see Petty (1990) for a general discussion on this problem). It is difficult to verify that the 'speckled' appearance (between 0° and 30°S) of the Goodberlet wind-speed field is actually due to a wind-speed effect. Comparisons with ERS-1* scatterometer data for the same date and the same area suggest that the spatial variability of the wind-speed field is lower than that observed in Fig. 10(c) (C. Gaffard, personal communication). However, more work is needed to confirm these preliminary results. In the 1DVAR approach, the background wind speed is known with a good accuracy (2 m s⁻¹). As a consequence, the wind-speed field retrieved with 1DVAR is close to the ECMWF background. We are conscious that it is difficult to demonstrate that we improve the accuracy of the wind speed without comparing the 1DVAR retrieved wind speed with independent wind measurements. The theoretical standard deviation of 1DVAR-retrieved wind speed varies between 1.6 m s⁻¹ and 0.5 m s⁻¹ for low to high wind speed. This last value is believed to be underestimated owing to the very simple approximation used for the sea-foam emissivity. The modelling of the sea-surface emissivity/scattering has been identified as one of the most critical areas for the success of a 1DVAR method for a SSM/I-like instrument. The sea-surface model described in this paper gives sensible results, as no unreasonable feature appears in the retrieved fields.

The present method is believed to be the first attempt to retrieve CLW from SSM/I and collocated NWP cloud fields. The main advantage of using a NWP cloud field is that the vertical location of the cloud, the phase mixing (ice and liquid), the temperature and humidity inside the cloud are a priori defined in a consistent manner. The retrieved fields are almost insensitive to the value of the background CLW. The theoretical CLW errors have been found to vary between 0.02 kg m⁻² and 0.1 kg m⁻² depending mainly on the wind-speed conditions, the upper bound being observed for large wind speed (20 m s⁻¹). The validation of CLW still remains an open question because of the lack of independent accurate ground truth. However, the retrieved humidity profile, WS and CLW are the most probable solution which explains the observed radiances. This is obviously not checked when regression-type algorithms are used for retrieving each variable separately. A threshold on the value of the cost function at the end of the minimization has been shown to be a simple and efficient quality control.

We have assumed in this study that humidity and cloud forecast errors are uncorrelated in the absence of any information about the true correlations. The drawback of this assumption is that the 'coherence' between cloud and humidity may be lost during the retrieval, i.e. a cloud may persist even if the humidity has been significantly reduced. A simple and attractive solution for controlling the coherence between cloud and humidity

* European Remote Sensing Satellite.

could be, for instance, to add an extra term to the cost function (as it has been done for the control of supersaturation) in order to force the liquid water to appear and disappear above and below a certain relative humidity. So far this constraint has not been implemented but the solution presented above will be tested in future developments of the 1DVAR method.

Several problems have been identified which should receive further attention for using the full benefits of this method for NWP, such as the tuning of the radiative-transfer model, a better estimation of the biases, and an assessment of the **F** off-diagonal elements. However, in order to do so, SSM/I data have to be inverted for a large number of orbits in order to have statistically robust results. Since the first version of the scheme used in this study, significant progress has been made in developing a fast radiative-transfer model and its adjoint. The first results obtained with this fast model suggest that the processing of SSM/I data in real time with 1DVAR can be contemplated.

ACKNOWLEDGEMENTS

I am grateful to Dr J. R. Eyre (lately ECMWF, now UK Meteorological Office) for invaluable suggestions in the earlier stages of this work. I wish to thank Mr Erik Andersson (ECMWF) for providing the collocation software between SSM/I and ECMWF fields and Dr A. P. McNally for his helpful background on TOVS-1DVAR. I am also grateful to Dr A. Hollingsworth for his comments on the manuscript.

REFERENCES

- | | | |
|--|------|---|
| Alishouse, J. C., Snyder, S. A., Vongsathorn, J. and Ferraro, R. R. | 1990 | Determination of oceanic precipitable water from the SSM/I. <i>IEEE Trans. Geosci. Remote Sensing</i> , 28 , 5, 811–816 |
| Bloom, S. C. and Atlas, R. | 1991 | 'Assimilation of satellite surface wind speed data and its impact on NWP'. Proceedings of the 9th AMS conference on numerical weather prediction, Denver, Colorado, October 1991 |
| Cox, C. and Munk, W. | 1954 | Measurements of the roughness of the sea surface from photographs of the sun's glitter. <i>J. Opt. Soc. Am.</i> , 44 , 11, 838–850 |
| Derber, J. C., Parrish, D. F., Wu, W. S., Pu, Z. and Rivzi, S. R. H. | 1994 | 'Improvements to the operational SSI global analysis system'. Pp. 149–150 in Proceedings of the 10th AMS conference on numerical weather prediction, Portland, Oregon, July 1994 |
| English, S. J., Guillou, C., Prigent, C. and Jones, P. J. | 1994 | Aircraft measurements of water vapour continuum absorption at millimetre wavelengths. <i>Q. J. R. Meteorol. Soc.</i> , 120 , 603–625 |
| Eyre, J. R. | 1989 | Inversion of cloudy satellite sounding radiances by nonlinear optimal estimation. I: Theory and simulation for TOVS. <i>Q. J. R. Meteorol. Soc.</i> , 115 , 1001–1026 |
| | 1991 | 'A fast radiative transfer model for satellite sounding systems'. ECMWF Tech Memo 176 |
| Eyre, J. R., Kelly, G. A., McNally, A. P., Anderson, E. and Persson, A. | 1993 | Assimilation of TOVS radiance information through one-dimensional variational analysis. <i>Q. J. R. Meteorol. Soc.</i> , 119 , 1427–1463 |
| Ferraro, R. R., Grody, N. C. and Marks, G. F. | 1994 | Effects of surface conditions on rain identification using the DMSP-SSM/I. <i>Remote Sensing Rev.</i> , 11 , 195–210 |
| Filiberti, M. A. | 1993 | 'Assimilation dans des modèles météorologiques de données en vapeur d'eau intégrée mesurées par radiométrie hyperfréquence spatiale'. PhD dissertation, Université Paris 7, UFR de Physique |
| Goodberlet, M. A. and Swift, C. T. | 1992 | Improved retrievals from the DMSP wind speed algorithm under adverse weather conditions. <i>IEEE Trans. Geosci. Remote Sensing</i> , 30 , 5, 1076–1077 |
| Greenwald, T. J., Stephens, G. L., Vonder Haar, T. H. and Jackson, D. L. | 1993 | A physical retrieval of cloud liquid water over the global oceans using the Special Sensor Microwave/Imager observations. <i>J. Geophys. Res.</i> , 98 , D10, 18471–18488 |
| Grody, N. C. | 1988 | Surface identification using satellite microwave radiometers. <i>IEEE Trans. Geosci. Remote Sensing</i> , 26 , 850–859 |

- Grody, N. C. 1991 Classification of snow cover and precipitation using the special sensor microwave imager. *J. Geophys. Res.*, **96**, D4, 7423–7435
- Guillou, C. 1994 'Etude du transfert radiatif dans l'atmosphère en micro-ondes, à partir d'observations radiométriques aéroportées'. PhD dissertation, Université Paris 7, UFR de Physique
- Hollinger, J. P. 1971 Passive microwave measurements of sea surface roughness. *IEEE Trans. Geosci. Electron.*, **9**, 3, 165–169
- Hollinger, J. 1991 'DMSP special sensor microwave/imager. Calibration/validation'. Naval Research Laboratory. Final Report, Volume 2. Washington DC
- Hollinger, J., Peirce, J. L. and Poe, G. A. 1990 SSM/I instrument evaluation. *IEEE Trans. Geosci. Remote Sensing*, **28**, 5, 781–790
- Keihm, S. J. 1992 'Atmospheric absorption from 20–32 GHz: radiometric constraints on the vapour and oxygen components'. Pp. 211–218 in Proceedings of the specialist meeting on microwave radiometry and remote sensing applications, Boulder, CO
- Kunkee, D. B. and Gasiewski, A. J. 1994 'Airborne passive polarimetric measurements of sea surface anisotropy at 92 GHz'. IGARSS '94 Proceedings
- Liebe, H. J. 1989 MPM—an atmospheric millimetre wave propagation model. *Int. J. Infrared and Millimetre Waves*, **10**, 6, 631–650
- Liu, W. T., Tang, W. and Wentz, F. J. 1992 Precipitable water and surface humidity over global oceans from special sensor microwave imager and European Centre for Medium-Range Weather Forecasts. *J. Geophys. Res.*, **97**, C2, 2251–2264
- Lorenc, A. C. 1981 A global three-dimensional multivariate statistical analysis scheme. *Mon. Weather Rev.*, **109**, 701–721
- Matveev, L. T. 1984 *Cloud dynamics*. D. Reidel Publishing Company, Dordrecht, Holland
- Monohan, E. C. and Muircheartaigh, I. Ó. 1980 Optimal power-law description of oceanic whitecap coverage dependence on wind speed. *J. Phys. Oceanogr.*, **10**, 2094–2099
- NAG 1991 'NAG Fortran Library Manual, Mark 15'. (Available from NAG Ltd., Oxford, UK)
- Petty, G. W. 1990 'On the response of the special sensor microwave/imager to the marine environment—implications for atmospheric parameter retrievals'. PhD dissertation, University of Washington
- Phalippou, L. 1991 'Simulation d'images obtenues par radiométrie micro-onde: application au sondage atmosphérique pour Météosat seconde génération. PhD dissertation, available from Ecole Nationale Supérieure des Télécommunications, Paris
- 1992 'Comparison between SSM/I and ECMWF total precipitable water'. Pp. 22–26 in Proceedings of the specialist meeting on microwave radiometry and remote sensing application. Ed. E. R. Westwater. Boulder, Colorado. June 1992
- 1993 'A microwave radiative transfer model'. ECMWF Tech Memo 190
- Prigent, C. and Abba, P. 1990 Sea surface equivalent brightness temperature at millimetre wavelength. *Annales Geophysicae*, **8**, 627–634
- Prigent, C., Sand, A., Klapisz, C. and Lemaitre, Y. 1994 Physical retrieval of liquid water contents in a North Atlantic cyclone using SSM/I data. *Q. J. R. Meteorol. Soc.*, **120**, 1179–1207
- Rodgers, C. D. 1976 Retrieval of atmospheric temperature and composition from remote sensing of thermal radiation. *Rev. Geophys. Space Phys.*, **14**, 4, 609–624
- Ruprecht, E., Fuhrhop, R. and Simmer, C. 1992 Statistical analysis of the interrelation of the different channel observations of DMSP–SSM/I. Pp. 276–280 in Proceedings of the specialist meeting on microwave radiometry and remote sensing applications, Boulder, CO
- Smith, P. M. 1988 The emissivity of sea foam at 19 and 37 GHz. *Trans. Geosci. Remote Sensing*, **26**, 5, 541–547
- Stoffelen, A. and Anderson, D. 1994 'The ECMWF contribution to the characterisation, interpretation, calibration and validation of ERS-1 scatterometer backscatter measurements and winds, and their use in numerical weather prediction models'. Final Report. ESA contract 9097/90/NL/BI
- Stogryn, A. 1967 The apparent temperature of the sea at microwave frequencies. *IEEE Trans. Antennas and Propag.*, **Ap-15**, 2, 278–286

- | | | |
|---|------|--|
| Stogryn, A. | 1972 | The emissivity of sea foam at microwave frequencies. <i>J. Geophys. Res.</i> , 77 , 9, 1658–1666 |
| Talagrand, O. | 1988 | 'Four-dimensional variational assimilation'. Pp. 1–30 in ECMWF seminar proceedings on data assimilation and the use of satellite data, Vol 2 |
| Tiedtke, M. | 1993 | Representation of clouds in large-scale models. <i>Mon. Weather Rev.</i> , 121 , 11, 3040–3061 |
| Ulaby, F. T., Moore, R. K. and Fung, A. K. | 1981 | <i>Microwave remote sensing</i> . Vol. 1: <i>Microwave remote sensing fundamentals and radiometry</i> . Addison-Wesley Publishing Company Inc. |
| | 1986 | <i>Microwave remote sensing</i> . Vol 3: <i>From theory to applications</i> . Artech House Inc. |
| Walter, S. J. | 1992 | 'The tropospheric microwave water vapour spectrum: uncertainties for remote sensing'. Pp. 203–210 in Proceedings of the specialist meeting on microwave radiometry and remote sensing applications, Boulder, CO |
| Wentz, F. J. | 1992 | Measurements of oceanic wind vector using satellite microwave radiometers. <i>IEEE Trans. Geosci. Remote Sensing</i> , 30 , 5, 960–972 |
| Westwater, E. R., Sorider, J. B. and Falls, M. J. | 1990 | Ground based radiometric observations of atmospheric emission and attenuation at 20.6, 31.65 and 90.0 GHz: a comparison of measurements and theory. <i>IEEE Trans. Antennas Propag.</i> , AP-38 , 10, 1569–1580 |
| Wilheit, T. T. | 1979 | A model for the microwave emissivity of the ocean's surface as a function of wind speed. <i>IEEE Trans. Geosci. Electron.</i> , GE-17 , 4, 244–249 |
| Wu, W. S. and Derber, J. C. | 1994 | Inclusion of SSM/I precipitable water observations in the NMC spectral statistical-interpolation analysis system. Proceedings of the 10th AMS conference on numerical weather prediction, Portland, Oregon, July 1994 |